Virtual Bronchoscopy for Quantitative Airway Analysis

A. P. Kiraly,[1] J. M. Reinhardt,[2] E. A. Hoffman,[2,3] G. McLennan,[4] and W. E. Higgins[5]

[1]Siemens Corporate Research, Princeton, NJ 08540 USA
[2]Department of Biomedical Engineering, University of Iowa, Iowa City, IA 52242 USA
[3]Department of Radiology, University of Iowa, Iowa City, IA 52242 USA
[4]Department of Internal Medicine, University of Iowa, Iowa City, IA 52242 USA
[5]Department of Electrical Engineering, Penn State University, University Park, PA 16802 USA

ABSTRACT

We propose a new quantitative method for detailed analysis of the major airways. Using a 3D MDCT chest image as input, the method involves three major steps: (1) segmentation of the airway tree, (2) extraction of the central-axis structure of the major airways, and (3) a novel improvement on the standard full-width half-maximum approach for airway-wall delineation. The method produces measurements for all defined tree branches. These measurements include various airway diameters and cross-sectional area values. To facilitate the examination of these measurements, we also demonstrate an integrated virtual-bronchoscopic analysis system that enables flexible interrogation of the airways. Of particular note are techniques for unraveling and viewing the topography of selected airways. A large series of phantom and human tests confirm the efficacy of our methods.

Keywords: virtual endoscopy, virtual bronchoscopy, airway analysis, MDCT,3D imaging, pulmonary imaging

1. INTRODUCTION

New multi-detector computed-tomography (MDCT) scanners produce very high-resolution 3D digital images of the human chest [1]. Such MDCT images permit detailed quantitative airway analysis enabling the physician to assess disease state and plan treatment. This paper focuses on local measurements along a selected airway branch. In particular, we consider the lumen cross-sectional area and various airway diameters along a branch.

Accurate quantitative measurement of airway structures in MDCT images can be challenging for several reasons. First, structures are subject to partial volume effects and are distorted by the scanner's point spread function (PSF) [2–4]. For example, pure air voxels have values near -1000 HU and pure soft-tissue (or airway wall) voxels have values near 0 HU. Voxels straddling air and airway walls, however, typically have values somewhere between -1000 HU and 0 HU. As a second challenge, insufficient spatial resolution can cause stenosed airways or thin airway walls to appear broken or discontinuous. Finally, image-reconstruction artifacts, such as those introduced by a sharp high-frequency kernel, can introduce discontinuities in airways [5].

Previously proposed methods for computing airway-branch measurements involved some variant of the following three-stage approach [4, 6–12]: (1) extract (segment) the airway of interest or entire airway tree from the given image data set; (2) compute a centerline (central axis) for the airway of interest; (3) derive the desired measurements for discrete sites along the airway centerline. Three issues limit the applicability of these methods: (1) only the binary-valued segmented airway is used to compute the measurements [6–10, 12]; (2) excessive human interaction is required to derive the measurements [6–8, 12]; (3) measurements are not made along an airway's central axis [4, 11]. This paper presents a method that draws upon both the segmented airway data and original gray-scale data, that requires no human interaction, and that derives measures along an accurate sub-voxel-level airway centerline.

Once airway measurements are computed, methods are needed for interrogating these measurements and for directly corroborating them to the given 3D MDCT image data. This task requires appropriate data-mining tools for systematically interacting with both the quantitative measurements and MDCT data [13, 14]. An individual airway branch depicts a detailed geometric cross-sectional profile locally along its length. In addition, the airway

*Correspondence: Email: weh2@psu.edu; WWW: http://mipl.ee.psu.edu/; Telephone: 814-865-0186; Fax: 814-863-5341.

tree exhibits a complex 3D structure when considered globally (i.e., when viewing the whole tree). Thus, suitable data-mining tools need to be integrated into a computer-based system that enables both local (airway) level and global (full chest) level interrogation. Previous systems suggested by researchers in the emerging field of virtual bronchoscopy (VB) offer some of the suitable tools, such as measurement plots, local oblique cross-sectional images, and unraveled "tube" views [15–20]. In this paper, we also present an interactive VB system tailored for airway measurement and subsequent visual interrogation.

2. MEASUREMENT METHODS

Given the original 16-bit gray-level MDCT Image I, four processing stages are performed:

1. Extract the airway tree to produce a segmentation image, I_S, using either an adaptive region growing or a hybrid morphological/region-growing technique. The segmentation techniques were validated previously and are discussed in detail in [21].
2. Use I_S to generate an airway tree model, $\mathbf{T} = (\mathbf{V}, \mathbf{B}, \mathbf{P})$, via the previously validated method described in detail in [20]. This model is comprised of a set of viewing sites $\mathbf{V}$, a set of branches $\mathbf{B}$, and a set of paths $\mathbf{P}$. Each path $\mathbf{p} \in \mathbf{P}$ is comprised of a series of connected branches. In turn, each branch $\mathbf{b} \in \mathbf{B}$ is comprised of a set of connected viewing sites. Finally, each viewing site $\mathbf{v} \in \mathbf{V}$ is comprised of a location $\mathbf{x}$ and direction $\mathbf{d}$; i.e., $\mathbf{v} = (\mathbf{x}, \mathbf{d})$. The location $\mathbf{x} = (x, y, z)$ specifies the viewing site position within an image; i.e., specifies a location within either the original image $I(\mathbf{x})$ or segmented airway tree image $I_S(\mathbf{x})$, where x, y, z correspond to coordinates of 3D space. The direction $\mathbf{d}$ specifies the heading of a branch at $\mathbf{v}$. The model $\mathbf{T} = (\mathbf{V}, \mathbf{B}, \mathbf{P})$ contains the centerline, or central-axis, structure of the airway tree captured by I_S.
3. Compute measurements for the major airways. Both global measurements, such as airway-tree hierarchical structure and branch angles, and local branch measurements are computed. Reference [22] gives details on the global measurements. This paper and subsection focus on the computation of local branch measurements.
4. Compute triangle surface representations for the endoluminal and extraluminal surfaces of the airway tree. We apply the standard Marching-Cubes algorithm in vtk to the segmented airway tree for this purpose [23].

Once these processing stages are completed, the user can interrogate the airway tree using the VB system. The remainder of this section discusses the method for Stage 3, computation of the local airway measurements.

A set of diameter and cross-sectional area measurements are computed for each viewing site $\mathbf{v} \in \mathbf{V}$. To begin this computation, local cross-sectional images, $I^{\mathbf{v}}$ and $I_S^{\mathbf{v}}$, perpendicular to $\mathbf{v}$, relative to direction $\mathbf{d}$, are derived from I and I_S; the centers of both of these cross-sectional images equals $\mathbf{x}$. $I^{\mathbf{v}}$, derived from I, contains the original gray-scale data for the airway and wall about the viewing site $\mathbf{v}$. $I_S^{\mathbf{v}}$, derived from I_S, contains only the binary segmented data from the (inner) airway lumen at $\mathbf{v}$. See Figure 1.

Given these cross-sectional images, the following measurements are computed: (1) minimum inner diameter; (2) maximum inner diameter; (3) inner diameter orthogonal to the minimum inner diameter; (4) minimum outer diameter; (5) maximum outer diameter; (6) cross-sectional area. For these measurements, the inner and outer diameters are delineated by the airway walls. An inner diameter refers to a distance across the airway lumen, while an outer diameter refers to a distance across the outer airway-wall boundaries circumscribing the airway.

The next step involves collecting values from these cross-sectional images along a series of rays. Per Figure 1b, two sets of a evenly spaced one-dimensional rays of length f are cast, where a is the total number of rays cast from the center of the cross-section, $\vec{r}_{si}$ equals the i^{th} ray derived from $I_S^{\mathbf{v}}$, and $\vec{r}_{gi}$ equals the i^{th} ray derived from $I^{\mathbf{v}}$. Note that the rays, $\vec{r}_{si}$ and $\vec{r}_{gi}$, are related in that they both contain data concerning the same portion of space. This correspondence, shown in Figure 1c, allows use of the segmentation data as a cue to the location of the inner airway wall within the gray-scale data. We assume that $a = 16$ (an even number), so that oppositely directed pairs of rays form line segments for diameter measurements. For example, the rays $\vec{r}_{g1}$ and $\vec{r}_{g9}$ form a line segment.

For each set of rays, $\vec{r}_{si}$ and $\vec{r}_{gi}$, the inner and outer radii are determined. Let $\vec{r}_{si}(x)$ and $\vec{r}_{gi}(x)$ denote the ray values at a distance x away from the center, where $0 \leq x \leq f$. Also, let l_i denote the location of the inner wall within the ray $\vec{r}_{gi}(x)$, and l_o denote the location of the outer wall within the ray $\vec{r}_{gi}(x)$. These indices also correspond to the inner and outer radii measurements.

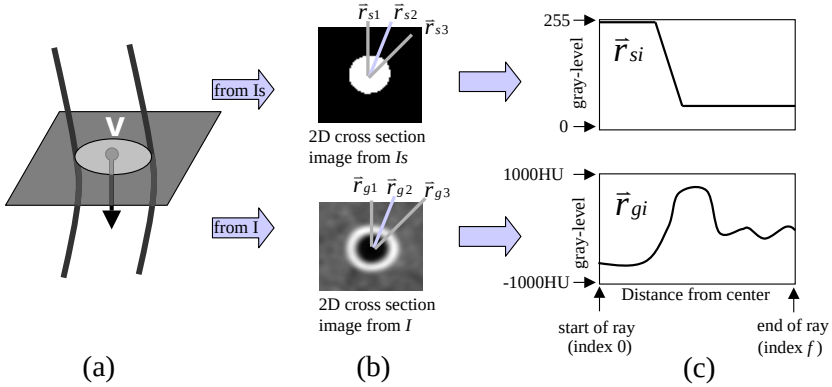

Figure 1. Outline of the steps used to acquire data along a ray at a viewing site **v**. First, cross-sections of the images I_S and I at the viewing site **v** are derived, as illustrated in (a). Trilinear interpolation is used to sample voxels in creating the two cross-section images shown in (b). A series of a rays is then sampled from the center of each image towards the edge. An increment of 0.25 pixels is used for each interpolated pixel. We use $a = 16$ rays. Image (c) shows an example of data collected along the rays $\vec{r}_{si}$ from the I_S-based cross-section (top) and $\vec{r}_{gi}$ from the I-based cross-section (bottom). The data along the ray is finite and indexed from 0 to the final index f. This data is then analyzed to provide inner and outer wall measurements.

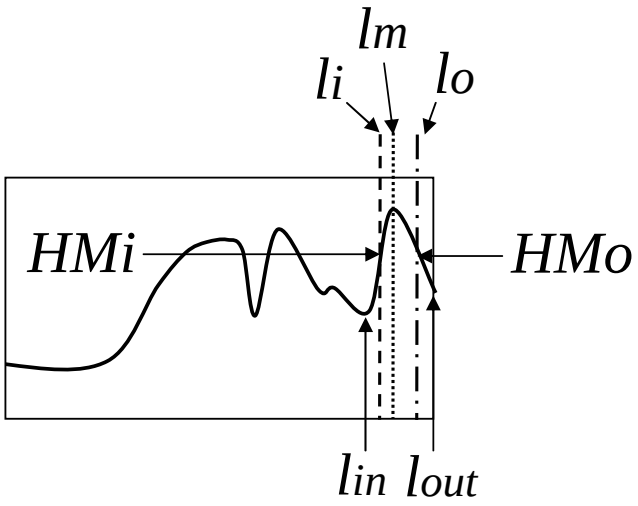

Figure 2. Schematic profile for a typical ray $\vec{r}_{g_i}$ for the standard FWHM method. The FWHM method's goal is to determine the inner and outer airway wall locations (indices), l_i and l_o, for ray $\vec{r}_{g_i}$ (see Figure 1). The horizontal axis signifies the distance along a ray, while the height refers to the image gray-scale at a ray point. The indices, l_{in} and l_{out}, refer to the local minima about the ray's global maximum l_m, while HM_i and HM_o are the intensity values of the inner and outer wall boundaries.

Before continuing, we first review the traditional FWHM method for computing the inner and outer wall locations, l_i and l_o — see Figure 2 [4]. Let $l_m = \arg\{\max_x, \vec{r}_{gi}\}$ (i.e., the location of the global maximum value of $\vec{r}_{gi}$), l_{in} equal the location of the local minimum of $\vec{r}_{gi}$ before l_m, and l_{out} equal the location of the local minimum of $\vec{r}_{gi}$ past l_m. In addition, let HM_i be the gray-level value for the inner wall; i.e., $HM_i = \vec{r}_{gi}(l_i)$, and let HM_o be the gray-level value for the outer wall, or $HM_o = \vec{r}_{gi}(l_o)$. The FWHM method begins by determining l_m, where

$$\vec{r}_{gi}(l_m) = \max_{i \in [0,\cdots,f]} \vec{r}_{gi}(i).$$

Next, the local-minima locations, l_{in} and l_{out}, along the inner and outer portions of $\vec{r}_{gi}$ about the maximum location l_m are found. The "half-maximum" values, used to denote the inner and outer wall boundaries, are then computed:

$$HM_i = \frac{\vec{r}_{gi}(l_m) + \vec{r}_{gi}(l_{in})}{2}, \quad HM_o = \frac{\vec{r}_{gi}(l_m) + \vec{r}_{gi}(l_{out})}{2}. \tag{1}$$

The next step involves finding where the ray reaches these gray-level values near l_m. The inner-wall location $l_i \in [l_{in}, l_m]$ and outer-wall location $l_o \in [l_m, l_{out}]$ are the ray indices that give the half-maximum values (1):

$$\vec{r}_{gi}(l_i) = HM_i \ , \ \vec{r}_{gi}(l_o) = HM_o.$$

Figure 2 shows the FWHM results for a sample ray. The standard FWHM method provides poor and misleading results when artifacts and noise corrupt the MDCT data, since an entire ray is searched for a global maximum.

To provide more robust wall-analysis along a ray, we propose two new techniques. These techniques, motivated by the standard FWHM technique, will be referred to as the **S**egmentation-**L**imited FWHM (FWHM$_{SL}$) and the **E**dge-cued **S**egmentation-**L**imited FWHM (FWHM$^E_{SL}$) techniques. See Figure 3. They provide more robust ways for determining l_m by drawing upon the ray $\vec{r}_{si}$ from the segmented image I_S. Define l_s as the location of the segmentation edge within $\vec{r}_{si}$; i.e., it is the location where the gray levels drop halfway (128) between the segmented (255) and background (0) levels. For both FWHM$_{SL}$ and FWHM$^E_{SL}$, this index is used to eliminate ray data from $l_s + w$ to f within $\vec{r}_{gi}$, as depicted in Figure 3, where w is a parameter. The ray $\vec{r}_{gi}$ is now limited from the original range $[0, f]$ to $[0, (l_s + w)]$. The FWHM$_{SL}$ technique is simply the application of the FWHM technique to this segmentation-limited ray. Figure 3a shows how the technique can be susceptible to errors due to the maximum determined. The FWHM$^E_{SL}$ method addresses the problem of window size dependence further. Instead of computing the maximum l_m based on the limited data set $[0, (l_s+w)]$, it is determined as the first local maximum near the segmentation edge l_s. The locations, l_i and l_o, are then determined just as in the FWHM method.

The crucial requirement for the w parameter for both techniques is that it must be large enough to include the wall within the ray. If parameter w is too small, the wall data will not be included and the measurements will be completely underestimated. If parameter w is too large, the technique degenerates to the standard FWHM technique. However, the FWHM$^E_{SL}$ technique's use of the segmentation edge makes it immune to situations were the w parameter is too large.

Once the inner and outer wall locations (radii), l_i and l_o, are determined, the diameter and cross-sectional area measurements are computed. For a given cross-sectional image (i.e., given viewing site), the various diameters about the cross-section are determined simply by taking the sums of the radii of oppositely directed rays. For this set of 8 diameters ($a = 16$ assumed), the minimum and maximum diameters are readily found. In addition, given the direction of the minimal inner diameter, the diameter in the orthogonal direction is readily found. Finally, the cross-sectional area is calculated by taking the sum of the area of the triangles formed from the rays. Let $(r_1, \cdots, r_a)$ be the radii for the inner wall determined from the a rays. Each of these lengths has an associated angle $(\alpha_1, \cdots, \alpha_a)$ determined by the direction of the rays. We convert these polar coordinates into Cartesian coordinates $(x_1, \cdots, x_a)$ and $(y_1, \cdots, y_a)$ based around the center $(0, 0)$ by

$$x_i = \cos(\alpha_i) \times r_i \ , \ y_i = \sin(\alpha_i) \times r_i.$$

Given this conversion, the following well-known formula is applied to compute the cross-sectional area [24]:

$$Area = \frac{(x_a \times y_0) - (x_0 \times y_a) + \sum_{n=1}^{a} (x_{n-1} \times y_n) - (x_n \times y_{n-1})}{2}$$

3. RESULTS

3.1. Phantom Data I

The accuracy of the airway measurement methods was first tested on phantom data of known dimensions (Figure 4) [4]. The data was reconstructed with the normal reconstruction kernel and consists of a Plexiglas phantom with seven tubes of known diameters inserted. The outer portion of the phantom was filled with potato flakes to simulate parenchymal tissue. The proposed methods were applied using both the hybrid and region growing

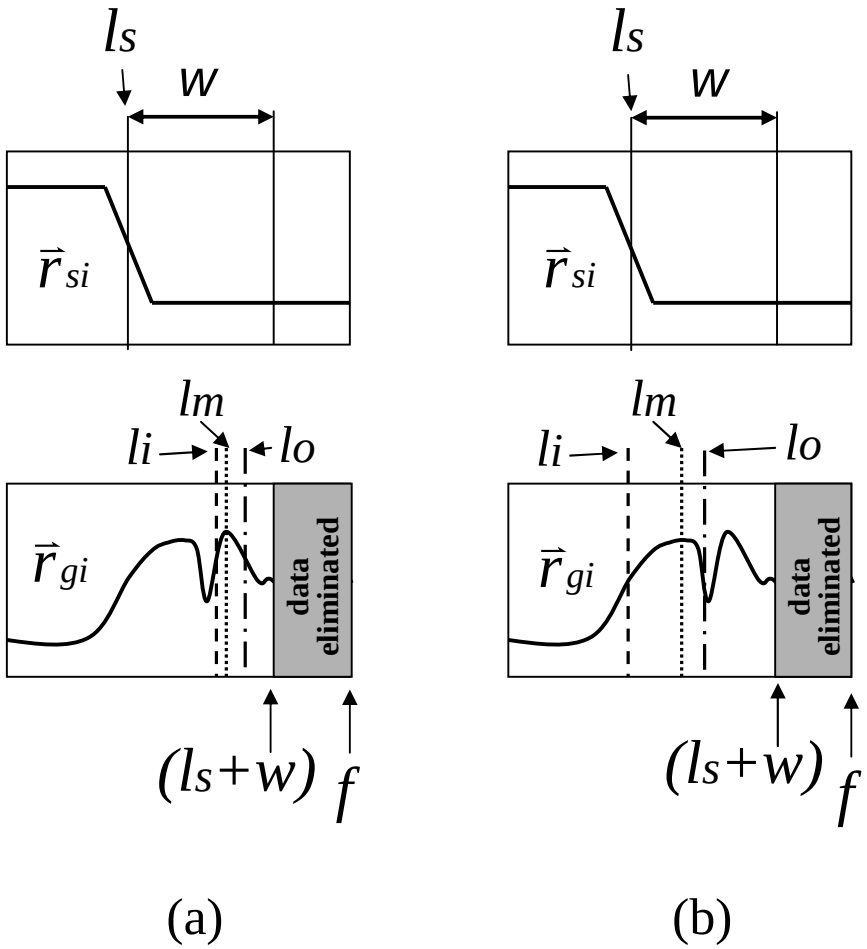

Figure 3. Schematic depiction of the proposed ray-analysis techniques: (a) FWHM_{SL}; (b) FWHM^{E}_{SL}. The edge location l_s and the parameter w are used to eliminate data from $\vec{r}_{gi}$. The FWHM_{SL} proceeds in the same manner as the standard FWHM method shown in Figure 2. The FWHM^{E}_{SL} method determines the local maximum near the location of l_s. The dotted line shows the located maximum l_m, the dashed line shows the located inner wall l_i, and the dash-dotted line shows the located outer wall l_o. The FWHM^{E}_{SL} technique is more independent of the w parameter, since the segmentation edge is used to determine the maximum. The figure demonstrates how the FWHM_{SL} can fail to find the correct wall, because of a global maximum. See text for additional details.

airway-tree segmentation methods of [21]. In addition, direct measurements on the segmented data were done for both segmentation methods. Parameter w was set to 2.61mm, since some of the walls were thick.

Measurement results are shown in Tables 1 and 2, while Table 3 lists the corresponding mean errors. The segmentation-based measurements are also included. The largest mean error of 0.98mm on average occurred in the measurements based on region-growing (RG) segmentation. Most of these measurements overestimated the diameters. The hybrid segmentation demonstrated the lowest average error for the inside diameters with a -0.02mm average error. However, two factors should be noted. First, this value is only the average of all measurements, both over and underestimations. Second, the segmentation has the same 0.29mm resolution as the image. Finally, the standard deviation was greater than for the proposed methods. Concerning the segmentations, the hybrid segmentation covered less area than the RG segmentation. This result, not typical for human CT data [21], occurred due to the high HU values created by the Plexiglas walls. The RG segmentations reached a gray level of -500HU to 0HU instead of the -850HU normally encountered with the human CT data. Hence, the RG segmentation extended beyond the air voxels causing the overestimation of the inner diameters for all but the smallest tube.

Both proposed methods obtained a mean error of -0.27mm with standard deviations of about 0.18mm for inner

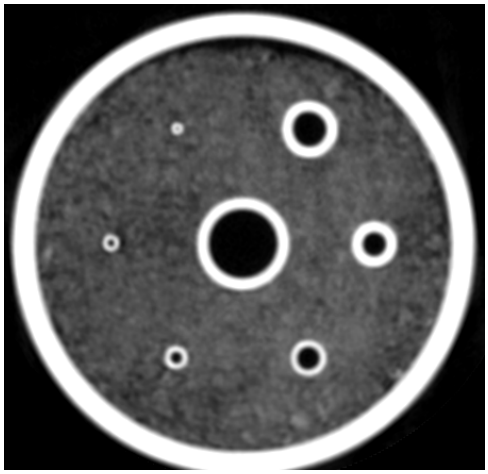

Figure 4. A transverse slice of the Plexiglas phantom used to evaluate the proposed airway-measurement methods [4]. A window level of (-1000HU to 0HU) was used to display the slice. The complete 3D phantom has image dimensions of $512 \times 512 \times 10$ with a resolution of $\Delta x = \Delta y = 0.29$mm and $\Delta z = 3.00$mm. The tubes were not exactly perpendicular to the transverse plane. Hence, the low Δz resolution plays a small factor in the accuracy of the measurements obtained.

Tube Number	Actual	Seg-RG	Seg-HYB	FWHM_{SL}	FWHM_{SL}^{E}
1	19.25	20.80 - 21.53	19.34 - 20.07	18.99 - 19.06	18.96 - 19.17
2	9.5	10.84 - 11.50	9.08 - 9.89	9.11 - 9.68	9.12 - 9.68
3	6.5	7.84 - 8.50	6.15 - 6.74	6.33 - 6.49	6.33 - 6.48
4	6.4	6.96 - 7.47	5.93 - 6.67	5.84 - 6.01	5.84 - 6.00
5	3.25	3.74 - 4.10	2.93 - 3.59	2.74 - 2.88	2.71 - 2.85
6	1.98	2.20 - 2.71	1.54 - 2.20	1.54 - 1.58	1.51 - 1.57
7	0.98	0.44 - 0.80	0.44 - 0.95	0.83 - 0.92	0.83 - 0.92

Table 1. Inner-wall diameter measurements for the Plexiglas tube phantom (units = mm). Each entry shows the range (minimum - maximum) of the diameters measured along a tube path. The direct segmentation measurements were applied to the region growing and hybrid segmentations, shown under "Seg-RG" and "Seg-HYB."

diameter measurements. Assuming a Gaussian error distribution, 95% of the values fell within 1.96 standard deviations of the mean. With these assumptions, the measurements fell within 0.35mm from the mean, with a bias of -0.27mm, 95% of the time. The Gaussian assumption will be used to analyze the remaining results. As noted in Figure 4, the low Δz resolution did play a small role in the accuracy of the results, since the tubes were not exactly perpendicular to the transverse plane. The outer-wall estimates of the proposed methods obtained a mean error of -0.07mm and -0.10mm, with standard deviations = 0.34mm for both cases. In conclusion, the proposed methods performed accurate measurements to the subvoxel level for both inner and outer diameter measurements. The possibility for errors with the Gaussian error assumption implies that inner diameter measurements errors are on the order of one voxel, and outer diameter measurement errors are on the order of two voxels. Note that each of these measurements are the result of two radii measurements.

3.2. Phantom Data II

A phantom model comprised of a hollow rubber cast made from a human airway tree and embedded in potato flakes was scanned at nine different orientations [25]. All images had a resolution of $\Delta x = \Delta y = 0.488$mm and $\Delta z = 0.50$mm. Each scanned image differs by a rotation in the horizontal and/or vertical planes. These rotations were $-15°$,0°, or $+15°$ for the horizontally plane and/or 0°,+15°, or +30° for the vertically plane to give nine different phantom scans. The purpose of these images was to test the reproducibility of the measurements at these different orientations. The proposed methods were applied using the hybrid segmentation method. Four different measurements were taken for each image: (1) Direct measurements on the segmentation; (2) FWHM_{SL}

Tube Number	Actual	FWHM_{SL}	FWHM^{E}_{SL}
1	25.5	24.93 - 25.12	24.88 - 25.09
2	15.6	14.94 - 15.44	14.94 - 15.43
3	12.6	12.11 - 12.25	12.12 - 12.24
4	9.7	9.82 - 9.96	9.83 - 9.95
5	6.3	6.40 - 6.55	6.40 - 6.55
6	4.45	4.63 - 4.84	4.58 - 4.76
7	3.3	3.39 - 3.51	3.38 - 3.49

Table 2. Outer-wall diameter measurements for the Plexiglas tube phantom (units = mm). Each element shows the range (minimum - maximum) of the diameters measured along the path within the tube. Only the FWHM-based approaches were used in this comparison since the segmentation does not provide outer-wall location.

Tube Number	Seg-RG	Seg-HYB	FWHM_{SL}	FWHM^{E}_{SL}
1	1.92	0.46	-0.23 / -0.48	-0.19 / -0.52
2	1.67	-0.02	-0.12 / -0.41	-0.10 / -0.45
3	1.67	-0.06	-0.09 / -0.42	-0.10 / -0.42
4	0.82	-0.10	-0.48 / 0.19	-0.48 / 0.19
5	0.67	0.01	-0.44 / 0.18	-0.47 / 0.13
6	0.48	-0.11	-0.42 / 0.28	-0.44 / 0.22
7	-0.36	-0.29	-0.11 / 0.15	-0.11 / 0.14
μ	0.98	-0.02	-0.27 / -0.07	-0.27 / -0.10
σ	0.82	0.23	0.17 / 0.34	0.18 / 0.34
Maximum	1.92	0.46	-0.09 / 0.28	-0.1 / 0.22
Minimum	-0.36	-0.29	-0.48 / -0.48	-0.48 / -0.52

Table 3. Differences between the average measurement and actual diameter measurements (units = mm). The inner and outer measurement errors are listed for the FWHM-based approaches and separated by a "/." The final three rows give the mean μ and standard deviation σ, the maximum difference value, and the the minimum difference value of the seven rows above.

with $w = 25$; (3) FWHM_{SL} with $w = 50$; and (4) FWHM^{E}_{SL} with $w = 50$.

The same path was manually selected from each computed tree. The individual branches along the path were then compared by using the average measurements of the middle 66% of the viewing sites. (The excluded sites are near the bifurcations and often give ill-defined cross-sectional images.)

Table 4 gives cumulative averages over all nine phantom scans. The standard deviations are low relative to the size of the individual measurements. See [22] for exhaustive results. Based on the average standard deviations (1.02), an error of 2 voxels was observed on average for diameter measurements. These values, however, actually ranged from 0.21 to 2.84. At worst, this corresponds to a 5.5 voxel difference. Additionally, this worst case only occurred in the maximum diameter determined for the airway in generation 2. All other standard deviations were close to or below 1.0. The standard deviations for the cross-sectional area measurements were greater, since they correspond to larger values and depend on several measurements. The relative ratio of the standard deviation to the actual value remained approximately the same. As the airways became smaller, the standard deviations remained approximately the same. Hence, measurement errors have a heavier influence on smaller airways.

The segmentation-based measurements had the lowest values of all measurements, because the segmentation tends to underestimate the inner wall. The FWHM^{E}_{SL} was greater by 2.25mm on average over the segmentation-based measurements and was roughly 1.5mm greater for the smaller airways having a diameter on the order of 1.7mm. The FWHM_{SL} method is limited by the segmentation to an even lesser extent, since the absolute maximum is taken. The increase of $w = 25$ to $w = 50$ also produces an average increase in measurement results, since more data is used from each ray, making it more likely that a larger maximum is identified. Note that the variations in these final results, with standard deviations ranging from 0.21mm to 2.84mm, can stem from the cumulative errors in the segmentation, tree model, and measurement process. Again, throughout these cumulative effects, an error of only $\pm$ 2 voxels was witnessed on average for the diameter measurements.

Method	area		max		min		ortho	
	μ	σ	μ	σ	μ	σ	μ	σ
FWHM_{SL}, $w = 50$	97.32	8.10	13.50	0.94	7.31	0.30	11.34	0.97
FWHM_{SL}, $w = 25$	88.37	7.53	12.36	1.02	7.25	0.30	10.66	0.90
FWHM^{E}_{SL}, $w = 50$	77.22	7.32	11.38	1.02	7.15	0.36	10.21	0.91
SEG-HYB	58.75	6.61	9.23	0.85	5.68	0.33	7.96	0.73

Table 4. Table of average mean μ and average standard deviation σ of measurements obtained using four different measurement methods over all nine orientations of the airway phantom. Table columns are as follows: area = cross-sectional area; max = maximum inner diameter; min = minimum inner diameter; ortho = diameter orthogonal to maximum diameter. All units are in mm, except mm^2 for cross-sectional area.

The results for outer-wall measurements for both methods were erratic, due to inconsistencies within the phantom's thick rubber wall. The rubber wall contained multiple, high-contrast minima and maxima. These created problems in the maxima determination. These situations, however, are less likely in human CT images, since the wall is generally not as thick and is more consistent. The problematic wall did reveal the superior robustness of the FWHM^{E}_{SL} in the inner wall determination. This robustness is due to the segmentation cue in the maxima determination. In conclusion, the methods demonstrated good invariance to orientation. The rubber phantom also revealed the superiority of the FWHM^{E}_{SL} method for interior diameter measurements in the event of irregular data.

3.3. Impact of Airway-Tree Segmentation Method

This subsection examines the influence of the airway-tree segmentation method on the FWHM^{E}_{SL} measurements. The FWHM^{E}_{SL} method was used, since it provides more robust inner-wall determination than the FWHM_{SL} method. It is also, however, more dependent on the segmentation. In this comparison, a human MDCT scan was segmented using both the region growing and hybrid methods [21]. (Reference [22] gives more exhaustive results.) A single tree model $\mathbf{T}$ obtained from the region-growing segmentation was used to avoid tree-model influences on the measurements. The trachea, left-main bronchus, and a peripheral branch were selected for comparison. Figure 5 gives measurement plots for these branches. Within the interior portion of a branch (away from the ill-defined branch-point regions), the measurements for the two methods tended to match well.

A Bland-Altman analysis (see Section 3.4) showed that the majority of the points fell within two standard deviations of the mean [22]. Concerning repeatability, our numerical results for the hybrid-based measurements varied within the following bounds in comparison to the region-growing-based measurements: (1) maximum diameter measurements — mean = 0.02mm, standard deviation = 0.16mm, measurements vary $\pm$0.32mm per case 95% of the time, maximum difference = 2.48mm; (2) minimum diameter measurements — mean = 0.03mm, standard deviation = 0.37mm, measurements vary $\pm$0.74mm per case 95% of the time, maximum difference = 5.61mm; (3) cross-sectional area measurements — mean = 0.29mm^2, standard deviation = 2.50mm^2, measurements vary $\pm 5.00\text{mm}^2$ per case 95% of the time, maximum difference = 21.37mm^2. Only 2% of the data points fell outside of two standard deviations of the mean, which was close to zero in all cases. Although the mean is expected to be exactly zero for independent measurements, it is nonzero due to the finite data set the results are based upon. The plotted points that are outside of two standard deviations tended to belong to the same measurement sets.

In conclusion, the airway-tree segmentation method has little effect on the mean measurements for the middle well-defined portions of the branches. The standard deviations suggest a 0.32mm (about 1 voxel) difference in the maximum diameter measurement. Although image segmentation has an influence, it is only on the order of the voxel resolution of the image.

3.4. Comparison with an existing airway-measurement system

A comparison between the proposed measurement method and an existing airway-analysis system is presented.

The existing airway-analysis system draws upon a semi-automatic method [6, 26]: (1) adjust the display of the image data to arrive at suitable view for the airway lumen; (2) use the FWHM technique to determine a gray-level threshold for 2D connected-component-labeling airway-lumen segmentation on a slice-by-slice basis; (3) apply a semi-automatic method to define the centerline of the segmented airway (human operator manually predefines the endpoints); (4) interpolate the resulting data to give a finer result; (5) compute the desired airway

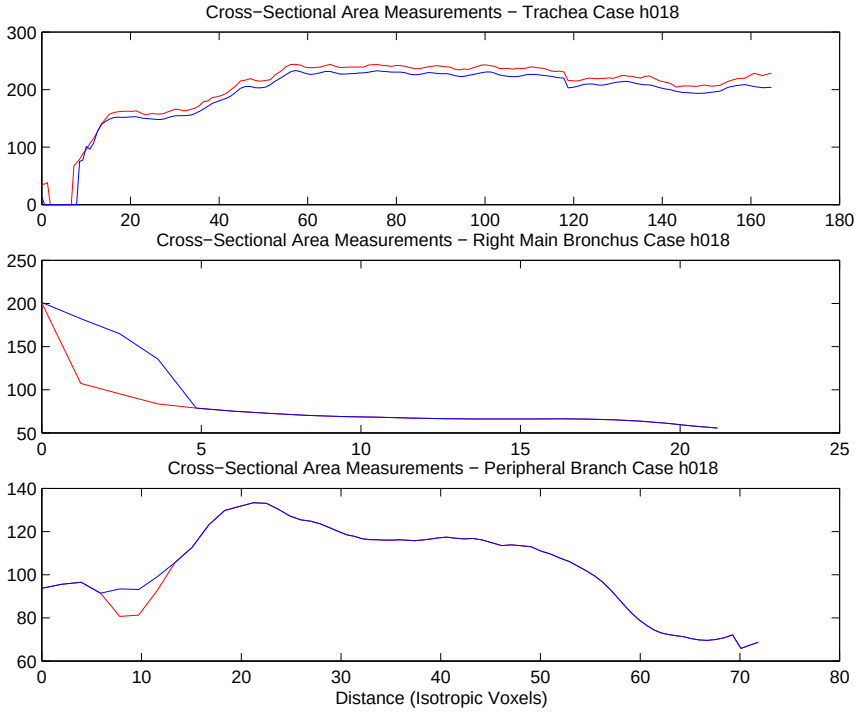

Figure 5. Impact of airway-tree segmentation method on airway cross-sectional area measurements for three branches in MDCT case h018 (448 512×512 slices, $\Delta x = \Delta y$ =0.57mm, Δz =0.60mm, Philips Mx8000 scanner). Results from the FWHM$^E_{SL}$ method for both the hybrid and region-growing segmentations are plotted on each figure. The vertical axis represents the cross-sectional area in mm^2. The horizontal axis represents the distance along a branch in isotropic voxel units. The top, middle, and bottom graphs show the results for the trachea, left main bronchus, and a peripheral branch.

measurements. This procedure has several drawbacks: (1) data is only computed for one selected branch; (2) all measurements are performed only on the segmented image; (3) the process requires on the order of two hours of human interaction (and this only gives results for one airway).

The two methods were compared for measurements made over 9 MDCT cases and a total of 17 branches: (1) 7 Philips Mx8000 cases, 14 branches total considered, $\Delta z = 0.60$mm, $\Delta x = \Delta y \approx 0.6$mm, 210 - 556 slices per scan; (2) 2 Toshiba Aquilion cases, 3 branches total considered, $\Delta z = 0.50$mm (280 slices) or 3.0mm (100 slices), $\Delta x = \Delta y \approx 0.6$mm. The FWHM$^E_{SL}$ approach with $w = 50$ was used in the comparison since it is more robust for internal wall measurements.

Before performing the comparison, we note in passing that the existing method exhibits significant variation in measurements when made at different times, because of the interaction necessary for image segmentation and centerline definition; see below for results. The proposed method, however, has no inter-trial variability, unless a different segmentation method is employed on the separate trials [22].

Figure 6 presents comparison results for a typical branch. ([22] gives more exhaustive results.) The major trend of the airway is agreed upon by each measurement method. The data from the existing system was not as complete for the proximal and distal ends in most cases. Hence, it was shifted to align with the data of the proposed method (this shifting was done visually for each data set).

A comparison of measurement trials was done using the graphical techniques and simple calculations of the Bland-Altman method [27, 28]. The Bland-Altman graph plots the differences in the measurements against their mean. This informative graph allows one to immediately see any kind of bias and measurement quantity dependencies and can help determine how future measurements would fair. Assuming that the differences are Gaussian distributed, 95% of the differences would fall within two (1.96) standard deviations σ of the mean μ. In order to appreciate this visually, the graph also plots the mean line along with lines for the mean $\pm$two (1.96)

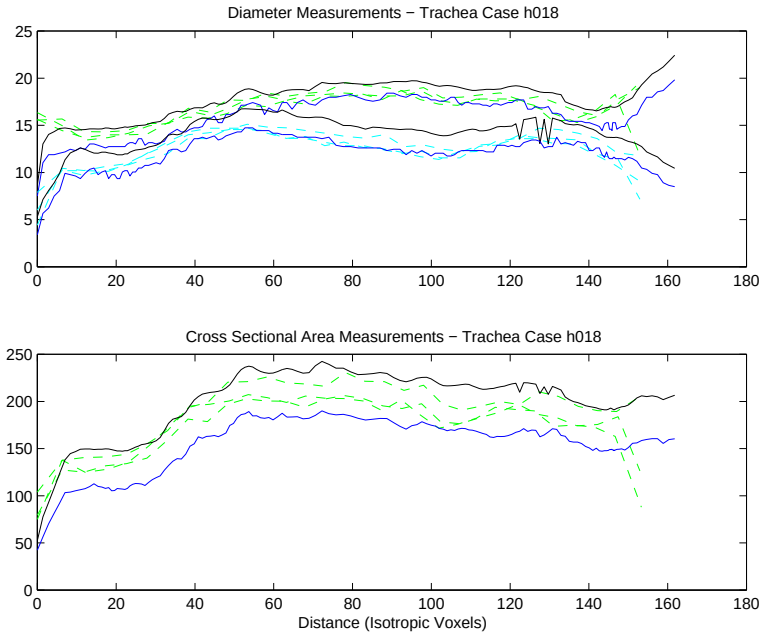

Figure 6. Graphs of proposed method and existing system results for diameter and cross-sectional area measurements within the trachea of Philips case h018. The upper graph shows both maximum and minimum diameter measurements, while the bottom graph shows the cross-sectional area measurements. The top solid lines represent data from the FWHM^E_{SL} method, while the bottom solid lines represent data from the initial segmentation. The dashed lines represent the existing system's measurements. In the case of diameter measurements, the bottom set of dotted lines represent the minimum diameter measurements. Note that multiple dashed lines occupy the same graph, since the existing system was run multiple times. The vertical axis in the upper graph is in mm, while the lower graph's vertical axis is in mm^2. The horizontal axes in both graphs are in units of isotropic voxels. The graphs show that all methods follow the same general trend.

standard deviations. Given the Gaussian assumption, we can then predict a limit on future measurements to be different by $\bar{d} \pm 1.96s$ from each other in 95% of the measurements, where $\bar{d}$ is the sample mean and s is the sample standard deviation.

We first considered the variability between three separate trial measurement runs of the existing system; these runs were done at different times for the various cases considered. The difference between individual measurements and the average were plotted against the measurement average; see Figure 7. The average mean and standard deviations for each set of measurements against their mean were computed from the Bland-Altman graphs to give the following aggregate results: (1) maximum diameter measurements — $\bar{d} = 0.15$mm, $s = 0.57$mm, measurements vary ± 1.14mm per case 95% of the time, maximum difference $= 4.31$mm; (2) minimum diameter measurements — $\bar{d} = 0.07$mm, $s = 0.52$mm, measurements vary ± 1.04mm per case 95% of the time, maximum difference $= 3.59$mm; (3) cross-sectional area measurements — $\bar{d} = 1.7\text{mm}^2$, $s = 9.14\text{mm}^2$, measurements vary $\pm 18.29\text{mm}^2$ per case 95% of the time, maximum difference $= 43.66\text{mm}^2$. The mean values should be zero in the ideal case. The absolute value of the average mean for all three cases against the total average was considered the mean in this listing to show experimental variability. Since we have a finite data set, the mean values are non-zero.

The Bland-Altman methodology was also used to compare the existing system and proposed method. The average of the previous method's repeated executions was used. The proposed method obtains significantly more measurement sites than does the existing system. Hence, numerous sites were eliminated from the proposed method. Only sites matching the positions along the existing system's measurements were kept. Linear interpolation was used in cases where the distances along the path did not match exactly with the discrete positions.

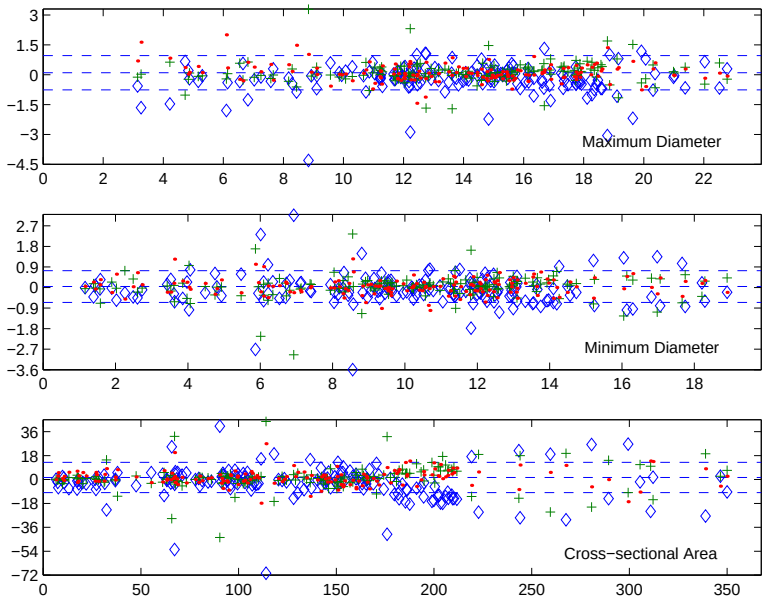

Figure 7. Bland-Altman graphs for the three runs measurements obtained from the existing system for all data sets. The top, middle, bottom graphs show the maximum diameter, minimum diameter, and cross-sectional area measurement results in units of mm, mm, and mm^2. The horizontal axis in all three graphs is in units mm along the branch. The difference between each individual measurement of a run and the average of all three runs for that same measurement is shown by each plotted point in the vertical axes. The horizontal axes show the average measurement obtained from the three runs. The difference data from each grouping of measurements is represented by diamonds, crosses, and dots. The dashed lines represent the mean $\bar{d}$ and twice (1.96) the standard deviation s from the mean for the data set with maximal variation from the total average.

The remaining sites were used for comparison. If we again assume that method differences follow a Gaussian distribution, we arrived at the following summary for measurement differences: (1) maximum diameter measurements — $\bar{d}$ = 0.74mm, s = 1.62mm, measurements +3.98mm to -2.51mm per case 95% of the time, maximum difference = 6.67mm; (2) minimum diameter measurements — $\bar{d}$ = 1.63mm, s = 1.41mm, measurements vary +4.46mm to -1.20mm per case 95% of the time, maximum difference = 6.36mm; (3) cross-sectional area measurements — $\bar{d}$ = 11.56mm^2, s = 27.25mm^2, measurements vary +66.07mm^2 to -42.94mm^2 per case 95% of the time, maximum difference = 104.26mm^2.

The proposed method resulted in a positive bias with larger measurement values on average. The segmentation-based existing method is more likely to underestimate the lumen's edge. Since the existing system's measurements are based on this segmentation, its results most likely tend towards an underestimate of diameters, which accounts for part of the bias. Results with other tested images all demonstrate this bias. The differences in diameter measurements are cumulative for the cross-sectional area measurements, since multiple diameters are used in its computation, which is also partly why the standard deviation for the cross-sectional area measurements is larger than those of the other two.

Taking into account the standard deviations of the measurements themselves, the standard deviations of the differences with the proposed method increases as was shown in [27]. The following shows the results after this consideration: (1) maximum diameter measurements — $\bar{d}$ = 0.74mm, s = 1.78mm, measurements vary +4.30mm to -2.82mm per case 95% of the time; (2) minimum diameter measurements — $\bar{d}$ = 1.63mm, s= 1.44mm, measurements vary +4.51mm to -1.25mm per case 95% of the time; (3) cross-sectional area measurements — $\bar{d}$ = 11.56mm^2, s = 28mm^2, measurements vary +67.56mm^2 to -44.44mm^2 per case 95% of the time. In summary, the proposed method contains a positive bias of about 0.74mm to 0.63mm, which can vary up to 3.56mm. The positive bias is most likely due to an underestimated segmentation used by the existing system. Considering the standard deviations of 1.78mm and 1.44mm between the two methods, the existing method has a standard deviation of 0.52mm and 0.57mm with itself on upon repeated measurements. This factor does influence the

computed differences. Regardless, both methods agreed on the same general trend of the measurements.

3.5. VB System Example

The original MDCT image I, airway-tree model $\mathbf{T}$, airway measurements, and the airway-surface representations serve as inputs to the the VB system. The VB system contains an integrated set of data-mining tools suitable for quantitative and visual airway assessment. Much of this system has been described in other publications [20, 21, 29] and was motivated by several previously proposed systems for virtual bronchoscopy and 3D medical image visualization [6, 18, 30–34].

The following basic tools, particularly suited for interrogating the airways, are available in our VB system: (1) Plot Tool, for viewing and interacting with the quantitative measurements along an airway [18, 20, 29]; (2) Cross-Section Tool, for viewing local oblique cross-sectional images along an airway centerline [18, 20, 29, 30]; (3) Tube Viewer, for interrogating various rendered forms of a mathematically straightened ("unravelled") airway branch [18]; (4) Sliding Thin-Slab Tool, for observing local thin-slab renditions of airway regions [20, 35]; and, of course, (5) an Endoluminal Renderer, for endoluminal ("virtual endoscopic") renderings inside an airway [18, 20, 21, 30, 31]. We have employed quantitative measurement plotting along an anatomical branch in early applications related to the airways [6, 18, 20] and coronary arteries [34]. Oblique cross-sectional image viewing was previously proposed in efforts related to 3D coronary arterial tree analysis [34], which in turn was inspired by and served as part of the Mayo Clinic's seminal ANALYZE system for 3D medical image visualization and analysis [32, 33]. Tube, or mathematically straightened, viewing was previously proposed by many researchers for the colon (e.g., [36]) and was probably first incorporated by the Mayo group in their ANALYZE system in a tool built for curved-section reformatting [33]. Thin-slab viewing was first proposed in [37]. Finally, endoluminal, or virtual-bronchoscopic, rendering is ubiquitous in VB systems; e.g., [15–17, 19].

Our VB system also has four supplemental tools enabling global viewing and interaction of a 3D data set: (1) Projection Tool, for visualizing weighted-sum or maximum-intensity projections [18, 20, 29–31]; (2) traditional transverse, sagittal, and coronal section viewing or (3) an alternate Cube Tool for viewing a combined display of these sections [29]; and (4) 3D Surface Tool, for visualizing a 3D airway tree rendering [20, 21, 29]. In addition to incorporating the newly proposed airway measurements described in the previous subsection, we introduce two novel tube-viewing methods for viewing the unravelled "tube" views of the airways: (1) a side-view of an internal volume-rendered half-surface cut away of the unravelled airway lumen; and (2) a topographic map of an airway's lumenal surface (horizontal axis is distance along the airway, while the vertical axis gives a 360^o mapping of the lumen topography). See [38] for more detail. The VB system offers full interactivity, for individual paths, branches, and viewing sites. Any interaction with one tool results in instant updates to any other tool.

Figures 8-9 give a composite example of the VB system for case h018. The patient previously had a constricted left main bronchus (LMB). A stent was inserted subsequently to open the airway. Figure 8 shows the following:

- upper left — coronal projection of MDCT scan, with precomputed centerlines superimposed on view. The highlighted centerline segment gives the portion focused on by the Tube Viewers and Plot Tool; the segment is delineated by viewing sites 138 and 1623. Small ball lies at selected viewing site 1525 within LMB.
- upper right — Three Tube Viewer renditions of the selected segment. Top tube gives a gray-scale cross-section at angle -90^o. Middle tube is a volume rendering of the endoluminal surface (threshold = -400) at angle = -90^o. Bottom tube depicts the flattened topographic surface map. All views have vertical width = 80 voxels and are at 5X magnification. Cross-section tube shows bright manifestation of the stent.
- lower left — Coronal front-to-back depth-weighted maximum slab view at selected viewing site, focus = 20, vision = 25, processing window = (-1024, 400), view window = (-1024, 400) [35]. The bright mesh-like structure of the stent is clearly visible.
- lower right — Endoluminal rendering at the selected viewing site.

Figure 9 shows the following additional views:

- Top — Cross-section views orthogonal (left view), horizontally oriented (middle), and vertically oriented (right) relative to the selected viewing site (situated at the center of these views). The bright structures circumscribing the dark lumen in these views corresponds to the stent.
- Bottom — 2D Plot of the maximum inner diameter versus distance along the segment. Selected viewing site appears as a ball. Notice that the stent does serve to equalize the diameter along the extent of the LMB. Plot discontinuity occurs in the airway segment transitioning from the trachea to the LMB.

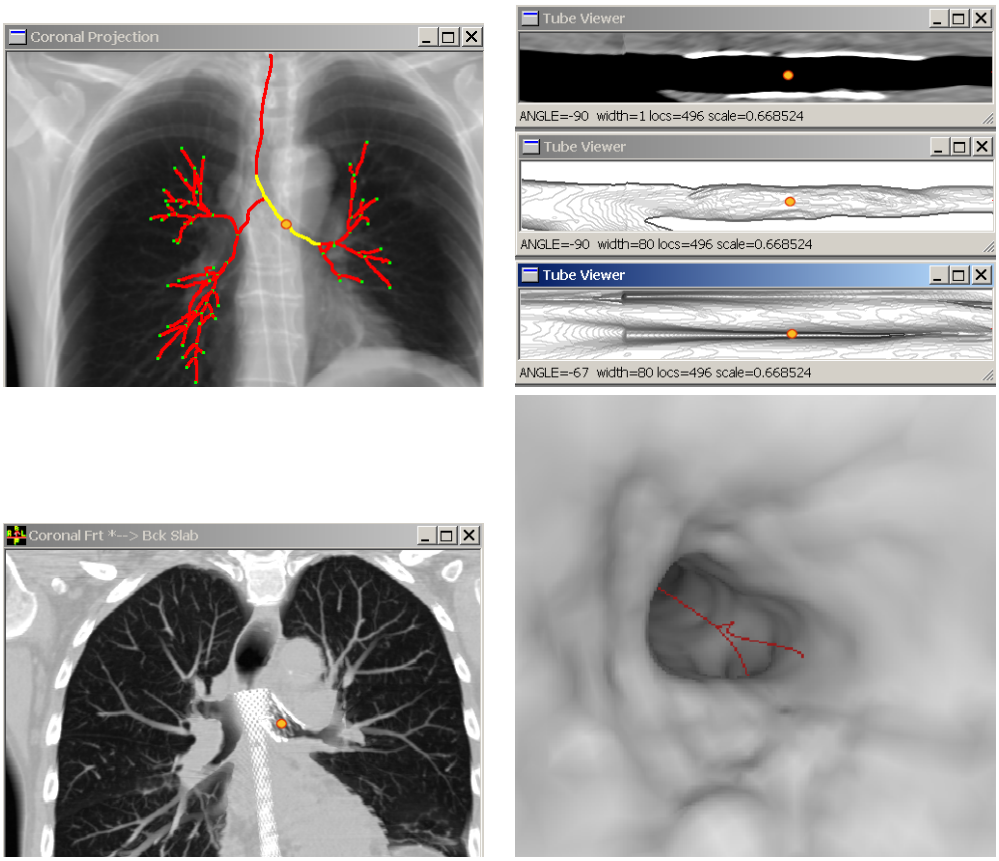

Figure 8. Part 1 - VB System focusing on left main bronchus for case h018.

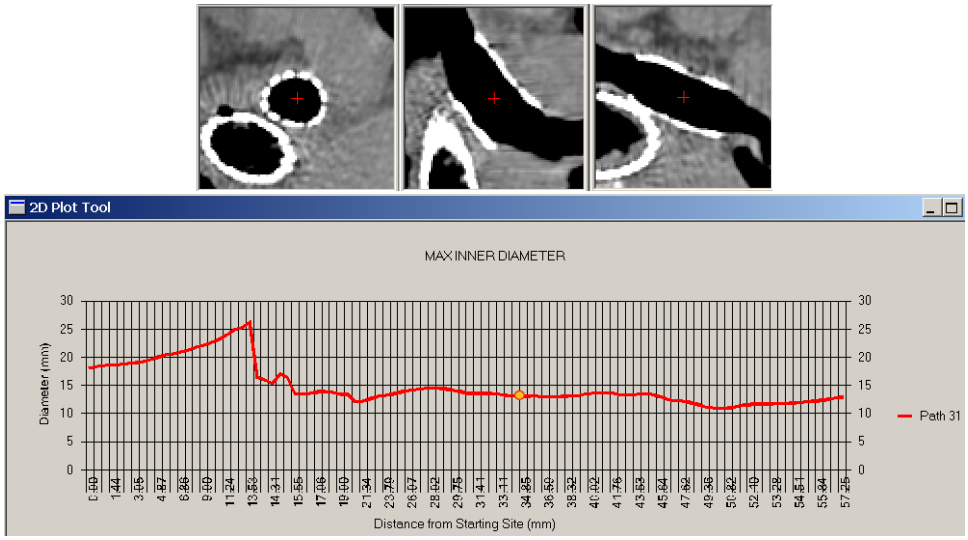

Figure 9. Part 2 - VB System focusing on left main bronchus for case h018.

4. DISCUSSION

We have presented a novel more robust airway measurement method. The method, which improves upon the existing full-width half-maximum technique, has been demonstrated to be robust and effective over a wide variety of phantom and human tests. The method also requires considerably less human interaction, gives more extensive results (results are given for a whole tree instead of just one selected branch), gives exactly reproducible results over different trials, and provides more detailed and robust measurements than an existing system for airway-branch measurement.

The measurement method also provides input to a integrated VB system. The VB system provides considerable capability for interrogating quantitative and visual airway data. Notably, the system incorporates two novel methods for viewing the unravelled airway lumenal surface. Further results for the measurement method can be seen in other publications More complete results on the impact of airway-tree segmentation appears in [22]. More comparison results between the proposed method and existing system, in addition to a comparison to purely manually derived measurements, appear in [22, 38]. These publications also give more Bland-Altman comparisons between the proposed method and existing system and other examples of using the VB system for airway analysis.

ACKNOWLEDGMENTS

This work was partially supported by grants #CA074325, #CA091534, and #CA094310 from the National Cancer Institute of the NIH, and by an NIH Bioengineering Research Partnership (NIH-HL-064368). We would like to thank Janice Cook-Granroth, who assisted in the semi-automatic measurements.

REFERENCES

1. E. A. Kazerooni, "High resolution CT of the lungs," *American Journal of Roentgenology* , pp. 501–519, Sept. 2001.
2. H. S. Choi, D. R. Haynor, and Y. Kim, "Partial volume tissue classification of multichannel magnetic resonance images – a mixel model," *IEEE Transactions on Medical Imaging* **10**, pp. 395–407, Sept 1991.
3. P. Santago and H. D. Gage, "Statistical models of partial volume effect," *IEEE Trans. on Image Processing* **4**, pp. 1531–1540, Nov 1995.
4. J. M. Reinhardt, N. D. D'Souza, and E. A. Hoffman, "Accurate measurement of intrathoracic airways," *IEEE Trans. Medical Imaging* **16**, pp. 820–827, Dec. 1997.
5. W. Kalender, *Computed Tomography: Fundamentals, System Technology, Image Quality, Applications*, Publicis MCD Verlag, Munich, 2000.
6. E. A. Hoffman, D. Gnanaprakasam, K. B. Gupta, J. D. Hoford, S. D. Kugelmass, and R. S. Kulawiec, "VIDA: An environment for multi-dimensional image display and analysis," *SPIE Proc. Biomed. Image Proc. and 3D Microscopy* **1660**, pp. 1–18, 1992.
7. I. Amirav, S. S. Kramer, M. M. Grunstein, and E. A. Hoffman, "Assessment of methacholine-induced airway constriction by ultrafast high-resolution computed tomography," *J. Applied Physiology* **75**(5), pp. 2239–2250, 1993.
8. Y. Nakano, S. Muro, H. Sakai, T. Hirai, K. Chin, M. Tsukino, K. Nishimura, H. Itoh, P. D. Pare, J. C. Hogg, and M. Mishima, "Computed tomographic measurements of airway dimensions and emphysema in smokers correlation with lung function," *Am. J. Respir. Crit. Care Med.* **162**, pp. 1102–1108, September 2000.
9. E. Sorantin, C. Halmai, B. Erdöhelyi, K. Palágyi, L. G. Nyúl, K. Ollé, B. Geiger, F. Lindbichler, G. Friedrich, and K. Kiesler, "Spiral-CT-based assessment of tracheal stenoses using 3-D skeletonization," *IEEE Trans. Medical Imaging* **21**, pp. 263–273, Mar. 2002.
10. R. D. Swift, A. P. Kiraly, A. J. Sherbondy, A. L. Austin, E. A. Hoffman, G. McLennan, and W. E. Higgins, "Automatic axis generation for virtual bronchoscopic assessment of major airway obstructions," *Computerized Medical Imaging and Graphics* **26**, pp. 103–118, Mar.-April 2002.
11. O. Saba, E. A. Hoffman, and J. M. Reinhardt, "Maximizing quantitative accuracy of lung airway lumen and wall measures obtained from X-ray CT imaging," *J. Applied Physiology* **95**, pp. 1063–1095, 2003.
12. S. Matsuoka, Y. Kurihara, Y. Nakajima, H. Niimi, H. Ashida, and K. Kaneoya, "Serial change in airway lumen and wall thickness at thin-section ct in asymptomatic subjects," *Radiology* , 10 December 2004.
13. J. Han and M. Kamber, *Data Mining: Concepts and Techniques*, Morgan Kauffman, San Francisco, 2001.
14. D. Keim, "Information visualization and visual data mining," *IEEE Trans. Visual. Comp. Graph.* **8**, pp. 1–8, Jan.-Mar. 2002.
15. D. J. Vining, K. Liu, R. H. Choplin, and E. F. Haponik, "Virtual bronchoscopy: relationships of virtual reality endobronchial simulations to actual bronchoscopic findings," *Chest* **109**, pp. 549–553, Feb. 1996.
16. G. D. Rubin, C. F. Beaulieu, V. Argiro, H. Ringl, A. M. Norbash, J. F. Feller, M. D. Dake, S. Napel, R. B. Jeffrey, and S. Napel, "Perspective volume rendering of CT and MR images: Applications for endoscopic imaging," *Radiology* **199**, pp. 321–330, May 1996.
17. R. M. Summers, "Navigational aids for real-time virtual bronchoscopy," *Am. J. Roentgenology* **168**, pp. 1165–1170, May 1997.

18. W. E. Higgins, K. Ramaswamy, R. Swift, G. McLennan, and E. A. Hoffman, "Virtual bronchoscopy for 3D pulmonary image assessment: State of the art and future needs," *Radiographics* **18**, pp. 761–778, May-June 1998.
19. G. Ferretti, I. Bricault, and M. Coulomb, "Virtual tools for imaging of the thorax," *Eur. Respir. J.* **18**, pp. 381–392, 2001.
20. A. P. Kiraly, J. P. Helferty, E. A. Hoffman, G. McLennan, and W. E. Higgins, "3D path planning for virtual bronchoscopy," *IEEE Trans. Medical Imaging* **23**, pp. 1365–1379, November 2004.
21. A. P. Kiraly, W. E. Higgins, G. McLennan, E. A. Hoffman, and J. M. Reinhardt, "Three-dimensional human airway segmentation methods for clinical virtual bronchoscopy," *Academic Radiology* **9**, pp. 1153–1168, September 2002.
22. A. P. Kiraly, *3D Image Analysis and Visualization of Tubular Structures*. PhD thesis, The Pennsylvania State University, 2003.
23. W. Schroeder, K. Martin, and B. Lorensen, *The Visualization Toolkit: An Object-Oriented Approach To 3D Graphics*, Prentice Hall, Upper Saddle River, N.J., 1997.
24. G. Bashein and P. R. Detmer, "Centroid of a polygon," in *Graphics Gems*, vol. IV, Academic Press, Inc., Boston, 1994.
25. J. Tschirren, K. Palágyi, J. M. Reinhardt, E. A. Hoffman, and M. Sonka, "Segmentation, skeletonization, and branchpoint matching—A fully automated quantitative evaluation of human intrathoracic airway trees," in *Lecture Notes in Computer Science*, T. Dohi and R. Kikinis, eds., vol. 2489, pp. 12–19, Springer-Verlag, Utrecht, October 2002.
26. G. McLennan, S. Shamsolkottabi, and E. A. Hoffman, "Assessment of major airway obstruction using image analysis of digital CT information," in *SPIE Medical Imaging 1996: Phys. and Funct. from Multidim. Images*, vol. 2709, pp. 197–208, 1996.
27. J. M. Bland and D. G. Altman, "Statistical methods for assessing agreement between two methods of clinical measurement," *Lancet* **i:307-310**, 1986.
28. K. Palagyi, J. Tschirren, and M. Sonka, "Quantitative analysis of three-dimensional tubular tree structures," in *Medical Imaging 2003: Image Processing. Edited by Sonka, Milan; Fitzpatrick, J. Michael. Proceedings of the SPIE, Volume 5032, pp. 277-287 (2003).*, pp. 277–287, May 2003.
29. R. Swift, A. Kiraly, A. Sherbondy, A. L. Austin, E. A. Hoffman, G. McLennan, and W. E. Higgins, "Automatic axes-generation for virtual bronchoscopic assessment of major airway obstructions," *Computerized Medical Imaging and Graphics* **26**, pp. 103–118, March-April 2002.
30. K. Ramaswamy and W. E. Higgins, "Interactive dynamic navigation for virtual endoscopy," *Computers in Biology and Medicine* **29**, pp. 303–331, Sept.-Oct. 1999.
31. M. L. Brady, K. Ramaswamy, R. Srinivasan, and W. E. Higgins, "Dynamic template-based method for 3D virtual-endoscopic exploration," *Optical Engineering* **38**, pp. 2162–2175, Dec. 1999.
32. R. A. Robb and C. Barillot, "Interactive display and analysis of 3-D medical images," **8**(3), pp. 217–226, Sept. 1989.
33. R. Robb and D. Hanson, "ANALYZE: A software system for biomedical image analysis," *Proc. First Int. Conf. Visualization in Biomed. Computing* , pp. 507–518, 1990.
34. W. Higgins, R. Karwoski, W. Spyra, and E. Ritman, "System for analyzing true three-dimensional angiograms," *IEEE Trans. Medical Imaging* **15**, pp. 377–385, June 1996.
35. J. Z. Turlington and W. E. Higgins, "New techniques for efficient sliding thin-slab volume visualization," *IEEE Transactions in Medical Imaging* **20**, pp. 823–835, Aug. 2001.
36. G. Wang, E. G. McFarland, B. P. Brown, and M. W. Vannier, "GI tract unraveling with curved cross sections," *IEEE Trans. Medical Imaging* **17**, pp. 318–321, April 1998.
37. S. Napel, G. D. Rubin, and R. B. Jeffrey, "STS-MIP, a new reconstruction technique for CT of the chest," *Journal of Computer Assisted Tomography* **17**(5), pp. 832–838, 1993.
38. A. P. Kiraly, J. M. Reinhardt, E. A. Hoffman, G. McLennan, and W. E. Higgins, "Virtual bronchoscopic methods for airway assessment," *Academic Radiology* , 2005. in preparation.